Journal of Computational Physics **154,** 310–341 (1999)
Article ID jcph.1999.6315, available online at http://www.idealibrary.com on IDEAL®

A Multigrid Semi-implicit Line-Method for Viscous Incompressible and Low-Mach-Number Flows on High Aspect Ratio Grids

Jan Vierendeels, Kris Riemslagh, and Erik Dick

Department of Flow, Heat and Combustion Mechanics, Universiteit Gent, Sint Pietersnieuwstraat 41, B-9000 Gent, Belgium
E-mail: Jan.Vierendeels@rug.ac.be, Kris.Riemslagh@rug.ac.be, Erik.Dick@rug.ac.be

Received July 16, 1998; revised May 17, 1999

Discretization of viscous incompressible and viscous low-Mach-number flows often leads to a system of equations, which is very difficult to solve. There are two reasons. First, the use of high aspect ratio grids results in a very numerically anisotropic behaviour of the diffusive and acoustic terms and second, in low-Mach-number flow, the ratio of the convective and acoustic eigenvalues of the inviscid system becomes very high. We implemented an AUSM based discretization method, using an explicit third-order discretization for the convective part and a line-implicit central discretization for the acoustic part and for the diffusive part. The lines are chosen in the direction of the grid points with shortest connection. The preconditioned semi-implicit line method is used in multistage form because of the explicit third-order discretization of the convective part. Multigrid is used as an acceleration technique. It is shown that the convergence is very good, independent of grid aspect ratio and Mach number.

Key Words: viscous incompressible flow; viscous low-Mach-number flow; multigrid method; high aspect ratio grid; preconditioning.

1. INTRODUCTION

Preconditioning of the incompressible [15, 17, 16] and compressible Navier–Stokes equations [2, 15, 7, 17, 9, 16] is used by many authors in order to accelerate convergence, especially for low-Mach-number flows. However, this technique does not always provide good results on high aspect ratio grids, because of the stiffness introduced by the numerically anisotropic behaviour of the diffusive and acoustic terms. For aspect ratios appropriate to the flow, preconditioning can help to eliminate this stiffness [9]. However, a more robust method consists in the use of an implicit line solver combined with multigrid [12].

0021-9991/99 $30.00

When standard flux-difference splitting is applied to the inviscid part of the compressible flow equations, the numerical scheme becomes very stiff for low Mach numbers [10]. Therefore the splitting scheme must be adapted, i.e., the system must be split according to its modified eigenvalues. The modified splitting is also necessary for accuracy [10, 8]. The reason is that the original flux-difference splitter is too dissipative in the streamwise direction for low Mach numbers since the dissipation term scales with $1/M$. Moreover, the use of a flux-difference splitter leads to a computationally expensive technique.

In our work, the stiffness due to the grid aspect ratio is removed by the use of line methods. The low-Mach-number stiffness together with the loss of accuracy is eliminated by an appropriate discretization of AUSM type (*a*dvection *u*pstream *s*plitting *m*ethod) and a local preconditioning technique. Multigrid is used as a convergence accelerator.

The discretization is AUSM simplified by taking the limit for vanishing Mach number and for constant density and extended by adding stabilization terms. There are two reasons for formulating the discretization scheme in this way. First, the flux definition is extremely cheap. It is much simpler than in a flux-difference scheme. It has a low cost comparable to the original AUSM [11]. Second, the discretization has, by construction, the correct physical behaviour for vanishing Mach number (low-Mach-number compressible flow) and incompressible flow.

The purpose of the paper is to present a scheme of high quality and high efficiency for low-speed applications with constant and varying density.

The method is illustrated with a backward facing step flow of an incompressible fluid and a compressible fluid at low speed and by thermally driven cavity flow.

2. GOVERNING EQUATIONS

The two-dimensional steady Navier–Stokes equations in conservative form for an incompressible fluid are

$$\begin{aligned} \frac{\partial u}{\partial x} + \frac{\partial v}{\partial y} &= 0, \\ \frac{\partial}{\partial x}u^2 + \frac{\partial}{\partial y}uv + \frac{\partial}{\partial x}p' &= \nu\left(\frac{\partial^2 u}{\partial x^2} + \frac{\partial^2 u}{\partial y^2}\right), \\ \frac{\partial}{\partial x}uv + \frac{\partial}{\partial y}v^2 + \frac{\partial}{\partial y}p' &= \nu\left(\frac{\partial^2 v}{\partial x^2} + \frac{\partial^2 v}{\partial y^2}\right), \end{aligned} \tag{1}$$

where u and v are the Cartesian components of velocity, p' is the kinematic pressure ($p' = p/\rho$), p is the pressure, ρ is the density, and ν is the kinematic viscosity.

The set of equations (1) can be written in system form as

$$\frac{\partial F_c}{\partial x} + \frac{\partial F_a}{\partial x} + \frac{\partial G_c}{\partial y} + \frac{\partial G_a}{\partial y} = \frac{\partial F_v}{\partial x} + \frac{\partial G_v}{\partial y},$$

where F_c and G_c are the convective fluxes, F_a and G_a are the acoustic fluxes, and F_v and G_v are the viscous fluxes,

$$F_c = \begin{bmatrix} 0 \\ u^2 \\ uv \end{bmatrix}, \qquad F_a = \begin{bmatrix} u \\ p' \\ 0 \end{bmatrix}, \qquad F_v = \begin{bmatrix} 0 \\ \nu\frac{\partial u}{\partial x} \\ \nu\frac{\partial v}{\partial x} \end{bmatrix},$$

and

$$G_c = \begin{bmatrix} 0 \\ uv \\ v^2 \end{bmatrix}, \qquad G_a = \begin{bmatrix} v \\ 0 \\ p' \end{bmatrix}, \qquad G_v = \begin{bmatrix} 0 \\ \nu \frac{\partial u}{\partial y} \\ \nu \frac{\partial v}{\partial y} \end{bmatrix}.$$

A distinction is made between the convective and acoustic parts of the inviscid flux vector because a different spatial and temporal discretization will be used for these parts.

3. DISCRETIZATION

Figure 1 shows a rectangular grid with constant mesh size Δx and Δy (Cartesian grid). The control volumes are centerd around the vertices of the grid.

The discretization of the convective flux is based on velocity upwinding,

$$F_{c_{i+1/2}} = u_{i+1/2} \begin{bmatrix} 0 \\ u \\ v \end{bmatrix}_{L/R}, \qquad G_{c_{j+1/2}} = v_{j+1/2} \begin{bmatrix} 0 \\ u \\ v \end{bmatrix}_{L/R}, \tag{2}$$

where

$$(\cdot)_{L/R} = \begin{cases} (\cdot)_L & \text{if } u_{1/2} > 0 \\ (\cdot)_R & \text{otherwise} \end{cases}$$

and

$$u_{i+1/2} = \frac{u_i + u_{i+1}}{2}, \qquad v_{j+1/2} = \frac{v_j + v_{j+1}}{2}.$$

We use a short notation for the subscripts. For instance $u_{i,j}$ is denoted by u_i or u_j and $u_{i,j+1}$ is denoted by u_{j+1}. The subscript which is not shifted with respect to i or j is omitted (Fig. 1).

The left (L) and right (R) values are computed with the Van Leer-κ approach,

$$\begin{aligned} q_L &= q_i + \frac{1}{4}[(1+\kappa)(q_{i+1} - q_i) + (1-\kappa)(q_i - q_{i-1})], \\ q_R &= q_{i+1} - \frac{1}{4}[(1+\kappa)(q_{i+1} - q_i) + (1-\kappa)(q_{i+2} - q_{i+1})], \end{aligned} \tag{3}$$

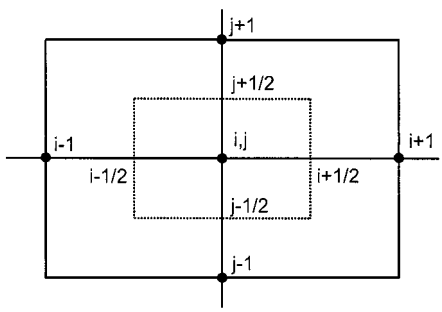

FIG. 1. Vertex-centerd control volume.

with $\kappa = 1/3$ for third-order accuracy. For a first-order approach the left and right values would be

$$q_L = q_i, \qquad q_R = q_{i+1}.$$

q stands for any of the three state variables u, v, or p.

The acoustic flux is discretized in the central way:

$$F_{a_{i+1/2}} = \begin{bmatrix} u \\ p' \\ 0 \end{bmatrix}_{i+1/2}, \qquad G_{a_{j+1/2}} = \begin{bmatrix} v \\ 0 \\ p' \end{bmatrix}_{j+1/2}.$$

The discretization of the convective and acoustic terms corresponds with the original AUSM-scheme [11] if the energy equation is omitted, a constant density is assumed, and the Mach number is going to zero.

The viscous flux is also discretized in the central way:

$$F_{v_{i+1/2}} = \begin{bmatrix} 0 \\ \nu \frac{u_{i+1} - u_i}{\Delta x} \\ \nu \frac{v_{i+1} - v_i}{\Delta x} \end{bmatrix}, \qquad G_{v_{j+1/2}} = \begin{bmatrix} 0 \\ \nu \frac{u_{j+1} - u_j}{\Delta y} \\ \nu \frac{v_{j+1} - v_j}{\Delta y} \end{bmatrix}.$$

Since the pressure term is discretized in the central way, pressure stabilization is needed. In the original AUSM-scheme there is a lack of pressure stabilization for Mach number going to zero. Therefore a pressure-velocity coupling was added in a newer version of the AUSM-scheme suitable for all speeds [6]. This pressure-velocity coupling consists of an artificial diffusion added to the mass flux. As discussed by Edwards and Liou [6], this term should scale inversely with the velocity magnitude. The same scaling of pressure-velocity coupling is present in the preconditioned Roe scheme [17] or in the flux-difference splitting for incompressible Navier–Stokes equations [5]. This pressure-velocity coupling introduces a pressure diffusion in the continuity equation and an upwinding of the pressure derivative in the momentum equations. However, the upwinding is only needed for high-speed compressible flow.

Taking into account the previous remarks, only an artificial dissipation term for the pressure is added in the continuity equation in the following way,

$$F_{d_{i+1/2}} = \begin{bmatrix} \delta \frac{p'_{i+1} - p'_i}{\beta_x} \\ 0 \\ 0 \end{bmatrix}, \qquad G_{d_{j+1/2}} = \begin{bmatrix} \delta \frac{p'_{j+1} - p'_j}{\beta_y} \\ 0 \\ 0 \end{bmatrix},$$

where β_x and β_y have the dimension of velocity. We have taken

$$\beta_x = w_r + \frac{2\nu}{\Delta x}, \qquad \beta_y = w_r + \frac{2\nu}{\Delta y},$$

where $\delta = 1/2$ and w_r is a reference velocity, either chosen to be a global velocity or a local velocity ($\sqrt{u^2 + v^2}$). For incompressible flow applications, we take a global reference velocity as the maximum velocity in the flow field. This results in a linear dissipation term with an advantage for implicit treatment of this term. For inviscid flow (i.e., $\nu = 0$), this term corresponds with the dissipation term introduced by the flux-difference splitting method for incompressible flow [5]. Following Weiss and Smith [17] and discussed by Merkle *et al.*

[13], β_x and β_y are treated in such a way that they scale with the local diffusion velocities $\nu/\Delta x$ and $\nu/\Delta y$ when these terms become important.

The complete flux vectors become

$$F = F_c + F_a - F_v - F_d, \qquad G = G_c + G_a - G_v - G_d.$$

4. TIME-MARCHING METHOD

In this study we use a time-marching method in order to reach the steady state solution of the incompressible Navier–Stokes equations. Since the discretization of the fluxes will be partly explicit and partly implicit, we do not consider a transformation into the primitive form of the equations. Applying the artificial-compressibility method to the conservative form of the inviscid part of the Navier–Stokes equations gives

$$\Gamma \frac{\partial Q}{\partial \tau} + \frac{\partial F_c}{\partial x} + \frac{\partial F_a}{\partial x} + \frac{\partial G_c}{\partial y} + \frac{\partial G_a}{\partial y} = 0.$$

Q is the vector of variables $[p', u, v]^T$. The preconditioning matrix Γ is given by

$$\Gamma = \begin{bmatrix} \frac{1}{\beta^2} & 0 & 0 \\ 0 & 1 & 0 \\ 0 & 0 & 1 \end{bmatrix},$$

where β has the dimension of velocity. The eigenvalues of the inviscid part of the preconditioned system are given by

$$\lambda\left(\Gamma^{-1}\frac{\partial(n_x F + n_y G)}{\partial Q}\right) = w, w + c, w - c, \tag{4}$$

where $w = n_x u + n_y v$, $c = \sqrt{w^2 + \beta^2}$, and n_x and n_y denote an arbitrary direction with $n_x^2 + n_y^2 = 1$. If β is of the same order of magnitude as the convective speed, all eigenvalues are properly scaled in at least one direction.

This artificial-compressibility method will be used as a smoother for the multigrid, as is shown in the next section. The artificial-compressibility method belongs to the family of local preconditioning techniques. Local preconditioning is known to work well on isotropic grids [9], but not always on non-isotropic grids, with high aspect ratios. This will be shown in the Fourier analysis in the next section. It will also be shown that a semi-implicit discretization is needed in order to have a robust method suitable for high aspect ratio meshes.

4.1. *Stepping in Pseudotime*

A multistage stepping is used with four stages,

$$\begin{aligned} Q^{(0)} &= Q^n \\ Q^{(1)} &= Q^{(0)} + \alpha_1\, cfl\, \Delta Q^{(0)} \\ Q^{(2)} &= Q^{(0)} + \alpha_2\, cfl\, \Delta Q^{(1)} \\ Q^{(3)} &= Q^{(0)} + \alpha_3\, cfl\, \Delta Q^{(2)} \\ Q^{(4)} &= Q^{(0)} + \alpha_4\, cfl\, \Delta Q^{(3)} \\ Q^{n+1} &= Q^{(4)}, \end{aligned}$$

with $\{\alpha_1, \alpha_2, \alpha_3, \alpha_4\}$ equal to $\{1/4, 1/3, 1/2, 1\}$ and the *cfl*-number equal to 1.8. We denote this *cfl*-number as the global *cfl*-number of the method. The $\Delta Q^{(m)}$ of each stage is given by $\Delta Q^{(m)} = Q^{(m+1)^*} - Q^{(m)}$ where $Q^{(m+1)^*}$ is computed with the semi-implicit point method (10) or the semi-implicit line method (7).

The multistage semi-implicit method is accelerated with the multigrid technique. A full approximation scheme is used in a W-cycle with four or five levels of grids. The computation is started on the finest grid in order to show the full performance of the multigrid method. For the restriction operator, full weighting is used. The prolongation is done with bilinear interpolation. Two pre- and postrelaxations are done. The use of five levels of grids results in a cost of 32.375 work units for each multigrid cycle, when one work unit consists of a residual evaluation and an update, or a residual evaluation together with a restriction and a prolongation.

4.2. *Determination of the Pseudotime Step*

Consider a uniform Cartesian mesh with constant Δx, Δy. The time step $\Delta\tau$ on this mesh is computed as

$$\Delta\tau = \frac{1}{(u + c_x)/\Delta x + (v + c_y)/\Delta y},$$

with

$$c_x = \sqrt{(u^2 + \beta^2)}, \tag{5}$$

and

$$c_y = \sqrt{(v^2 + \beta^2)}. \tag{6}$$

Assume that the flow is inviscid and aligned to the x-direction, i.e., $v = 0$. If β is chosen in the order of u, then all three eigenvalues (4) have the same order of magnitude in the x-direction and all waves are convected into this direction with a *cfl*-number in the order of unity.

It must be stressed that if the allowable *cfl*-number becomes smaller, the convergence will break down. This happens for large grid aspect ratios. We define the grid aspect ratio g_{ar} for the Cartesian grid as

$$g_{ar} = \frac{\Delta x}{\Delta y}.$$

If g_{ar} is very large, then the allowable time step $\Delta\tau$ is equal to $\Delta y/c_y$ and the maximum allowable *cfl*-number in the x-direction is

$$cfl_x = \frac{(u + c_x)\Delta\tau}{\Delta x} = \frac{u + c_x}{c_y}\frac{1}{g_{ar}} \approx \frac{1}{g_{ar}}.$$

This will lead to a breakdown of the convergence. It is shown in the Fourier analysis that if the acoustic fluxes in the y-direction are discretized implicitly, the system stays stable if

the time step definition is changed into

$$\Delta\tau = \frac{1}{(u + c_x)/\Delta x + \omega_1 v/\Delta y},$$

where ω_1 is a scaling factor. If the flow is aligned to the x-direction, then cfl_x is equal to unity. If the viscous terms are becoming important, the von Neumann number determines the maximum allowable time step

$$\Delta\tau = \frac{\Delta y^2}{2v},$$

and cfl_x will become small.

If the viscous terms are also treated with a line-implicit method in the y-direction, then this von Neumann restriction on the time step disappears, and the cfl_x-number is again in the order of unity. It is obvious that the acoustic and viscous terms need an implicit treatment in the direction of the smallest grid distances. These parts consist of linear terms. The convective part is non-linear and if an explicit treatment is used for this part, no Jacobians have to be recomputed every time step in order to update the set of equations. An implicit treatment of the convective part on high aspect ratio grids is not really necessary because the ratio $(u/\Delta x)/(v/\Delta y)$ can have the same values on an anisotropic grid as on an isotropic grid with more alignment of the flow, where it is known that explicit methods work well (e.g., the GAMM-bump test case can be solved without explicit preconditioned methods, even in the low-speed limit [7]). Therefore, our strategy is a combination of an explicit local preconditioning method and an implicit line method for the acoustic and viscous terms in the direction of the smallest grid distances.

This semi-implicit line method for a grid with small cell dimensions in the y-direction is given by

$$\begin{aligned}
&\left(\frac{\Gamma}{\Delta\tau} + 2\omega_2 A_d + 2\omega_3 A_v\right)\left(Q^{(m+1)^*} - Q^{(m)}\right) + \frac{\partial F_c^{(m)}}{\partial x} + \frac{\partial F_a^{(m)}}{\partial x} \\
&\quad - (A_v + A_d)\left(Q_{i-1,j}^{(m)} - 2Q_{i,j}^{(m)} + Q_{i+1,j}^{(m)}\right) + \frac{\partial G_c^{(m)}}{\partial y} + \frac{\partial G_a^{(m+1)^*}}{\partial y} \\
&\quad - (B_v + B_d)\left(Q_{i,j-1}^{(m+1)^*} - 2Q_{i,j}^{(m+1)*} + Q_{i,j+1}^{(m+1)^*}\right) = 0,
\end{aligned} \tag{7}$$

where A_v, B_v, A_d, and B_d are

$$A_v = \begin{bmatrix} 0 & 0 & 0 \\ 0 & \frac{\nu}{\Delta x^2} & 0 \\ 0 & 0 & \frac{\nu}{\Delta x^2} \end{bmatrix}, \qquad B_v = \begin{bmatrix} 0 & 0 & 0 \\ 0 & \frac{\nu}{\Delta y^2} & 0 \\ 0 & 0 & \frac{\nu}{\Delta y^2} \end{bmatrix},$$

and

$$A_d = \begin{bmatrix} \frac{\delta}{\beta_x \Delta x} & 0 & 0 \\ 0 & 0 & 0 \\ 0 & 0 & 0 \end{bmatrix}, \qquad B_d = \begin{bmatrix} \frac{\delta}{\beta_y \Delta y} & 0 & 0 \\ 0 & 0 & 0 \\ 0 & 0 & 0 \end{bmatrix},$$

and where

$$\beta = \sqrt{u^2 + v^2} + \frac{2\nu}{\Delta x}, \tag{8}$$

and

$$\Delta\tau = \frac{1}{(u + c_x)/\Delta x + \omega_1 v/\Delta y}, \tag{9}$$

with c_x computed as in Eq. (5) with β given by (8).

The introduction of the factor ω_1 results in a different scaling of the convective velocity in the direction of the implicit lines (y-direction) with respect to the convective velocity in the x-direction. The introduction of the factors ω_2 and ω_3 allows a different scaling of the artificial damping term and the viscous terms with respect to the convective terms. The scaling factors ω_1, ω_2, and ω_3 are available for optimization of the smoothing rate of the method. This optimization is treated in the next section.

In (8) there is no viscous contribution from the y-direction and in (9) there is no acoustic contribution from the y-direction because these terms are treated implicitly in this direction.

In order to illustrate the performance of the method we also consider the semi-implicit point method. For this method the equations are given by

$$\begin{aligned}
&\left(\frac{\Gamma}{\Delta\tau} + 2\omega_2(A_d + B_d) + 2\omega_3(A_v + B_v)\right)\left(Q^{(m+1)^*} - Q^{(m)}\right) \\
&\quad + \frac{\partial F_c^{(m)}}{\partial x} + \frac{\partial F_a^{(m)}}{\partial x} - (A_v + A_d)\left(Q_{i-1,j}^{(m)} - 2Q_{i,j}^{(m)} + Q_{i+1,j}^{(m)}\right) \\
&\quad + \frac{\partial G_c^{(m)}}{\partial y} + \frac{\partial G_a^{(m)}}{\partial y} - (B_v + B_d)\left(Q_{i,j-1}^{(m)} - 2Q_{i,j}^{(m)} + Q_{i,j+1}^{(m)}\right) = 0,
\end{aligned} \tag{10}$$

where

$$\beta = \sqrt{u^2 + v^2} + \frac{2\nu}{\Delta x} + \frac{2\nu}{\Delta y}, \tag{11}$$

and

$$\Delta\tau = \frac{1}{(u + c_x)/\Delta x + (v + c_y)/\Delta y},$$

with c_x and c_y computed as in Eqs. (5) and (6) with β given by (11).

Also here we have introduced the scaling factors ω_2 and ω_3 for the scaling of the artificial damping term and the viscous terms. Since the acoustic terms are centrally discretized, these terms are treated explicitly in the semi-implicit point method.

5. FOURIER ANALYSIS

The schemes of the previous section are now analysed with the Fourier method. We assume a rectangular grid without stretching and with periodical boundary conditions. The

state Q can be written as the sum of the steady state solution $\bar{Q}$ and an error Ψ which is function of the pseudotime τ:

$$Q(x, y, \tau) = \bar{Q}(x, y) + \Psi(x, y, \tau). \tag{12}$$

The error can be written as a sum of Fourier waves. The Fourier component with wave number ω_x in the x-direction and wave number ω_y in the y-direction is written as

$$\psi_{\omega_x,\omega_y}(x, y, \tau) = \phi(\tau)e^{j(\omega_x x+\omega_y y)}, \tag{13}$$

where j stands for the imaginary unit. The substitution of Eq. (12) into the system of Eqs. (10) results in a system of equations for the error. The linear terms result in identical expressions. The quadratic terms need some explanation.

As an example, the error due to the quadratic term

$$\frac{\partial u^2}{\partial x}$$

is worked out. Using (2), the first-order discretization of this term is written for a positive velocity component u as

$$\frac{1}{\Delta x}\left(u_{i+1/2}u_i - u_{i-1/2}u_{i-1}\right). \tag{14}$$

For the non-linear terms we assume a uniform flow field. Then u can be written as

$$u_k = \bar{u} + \psi_k,$$

where k stands for any subscript and $\bar{u}$ is constant. Using the previous expression, Eq. (14) becomes

$$\frac{1}{\Delta x}\bar{u}\left(\psi_{i+1/2} - \psi_{i-1/2} + \psi_i - \psi_{i-1} + \mathrm{O}(\psi^2)\right).$$

By introducing Eq. (13), the coefficient of the term $e^{j(\omega_x x+\omega_y y)}$ can be written as

$$\phi(t)\bar{u}(\mathrm{ce}(\theta_x, \Delta x) + \mathrm{up}(\theta_x, \Delta x)),$$

where

$$\mathrm{ce}(\theta, \Delta s) = \frac{e^{j\theta} - e^{-j\theta}}{2\Delta s},$$

and

$$\mathrm{up}(\theta, \Delta s) = \frac{1 - e^{-j\theta}}{\Delta s}k(\theta),$$

with $\theta = \omega\Delta s$ and $k(\theta) = 1$ for the first-order upwind scheme. For the Van Leer-κ method (3), $k(\theta)$ is given by

$$k(\theta) = 1 + \frac{1}{4}[(1 + \kappa)(e^{j\theta} - 1) + (1 - \kappa)(1 - e^{-j\theta})].$$

Similar equations hold if the velocity component u is negative. For completeness we already define $\mathrm{vi}(\theta, \Delta s)$ needed for the viscous contributions and the artificial dissipation term as

$$\mathrm{vi}(\theta, \Delta s) = \frac{-e^{-j\theta} + 2 - e^{j\theta}}{\Delta s^2}.$$

Neglecting higher-order terms in the error component, the following system for the error has to be solved for each stage in the time-marching procedure

$$\hat{P}\Delta\Psi + \hat{C}\Psi = 0. \tag{15}$$

The Fourier symbol $\mathcal{F}(\theta_x, \theta_y)$ is then given by

$$\mathcal{F}(\theta_x, \theta_y) = -cfl\hat{P}(\theta_x, \theta_y)^{-1}\hat{C}(\theta_x, \theta_y).$$

The expressions for $\hat{P}$ are dependent on the time-marching method and are given below. The expression for $\hat{C}$ is given by

$$\hat{C} = \hat{A} + \hat{B}, \tag{16}$$

where $\hat{A}$ contains the convective term $\hat{A}_c$, the acoustic term $\hat{A}_a$, the diffusion term $\hat{A}_v$, and the artificial dissipation term $\hat{A}_d$ in the x-direction, and $\hat{B}$ contains the corresponding terms in the y-direction,

$$\hat{A} = \hat{A}_c + \hat{A}_a + \hat{A}_v + \hat{A}_d,$$
$$\hat{B} = \hat{B}_c + \hat{B}_a + \hat{B}_v + \hat{B}_d,$$

where

$$\hat{A}_c = \begin{bmatrix} 0 & 0 & 0 \\ 0 & \bar{u}\,(\mathrm{up}(\theta_x, \Delta x) + \mathrm{ce}(\theta_x, \Delta x)) & 0 \\ 0 & \bar{v}\mathrm{ce}(\theta_x, \Delta x) & \bar{u}\mathrm{up}(\theta_x, \Delta x) \end{bmatrix},$$

$$\hat{B}_c = \begin{bmatrix} 0 & 0 & 0 \\ 0 & \bar{v}\mathrm{up}(\theta_y, \Delta y) & \bar{u}\mathrm{ce}(\theta_y, \Delta y) \\ 0 & 0 & \bar{v}(\mathrm{up}(\theta_y, \Delta y) + \mathrm{ce}(\theta_y, \Delta y)) \end{bmatrix},$$

and

$$\hat{A}_a = \begin{bmatrix} 0 & \mathrm{ce}(\theta_x, \Delta x) & 0 \\ \mathrm{ce}(\theta_x, \Delta x) & 0 & 0 \\ 0 & 0 & 0 \end{bmatrix}, \qquad \hat{B}_a = \begin{bmatrix} 0 & 0 & \mathrm{ce}(\theta_y, \Delta y) \\ 0 & 0 & 0 \\ \mathrm{ce}(\theta_y, \Delta y) & 0 & 0 \end{bmatrix},$$

and

$$\hat{A}_v = \begin{bmatrix} 0 & 0 & 0 \\ 0 & \nu\mathrm{vi}(\theta_x, \Delta x) & 0 \\ 0 & 0 & \nu\mathrm{vi}(\theta_x, \Delta x) \end{bmatrix}, \qquad \hat{B}_v = \begin{bmatrix} 0 & 0 & 0 \\ 0 & \nu\mathrm{vi}(\theta_y, \Delta y) & 0 \\ 0 & 0 & \nu\mathrm{vi}(\theta_y, \Delta y) \end{bmatrix},$$

and

$$\hat{A}_d = \begin{bmatrix} \frac{\delta}{\beta_x}\mathrm{vi}(\theta_x, \Delta x)\Delta x & 0 & 0 \\ 0 & 0 & 0 \\ 0 & 0 & 0 \end{bmatrix}, \qquad \hat{B}_d = \begin{bmatrix} \frac{\delta}{\beta_y}\mathrm{vi}(\theta_y, \Delta y)\Delta y & 0 & 0 \\ 0 & 0 & 0 \\ 0 & 0 & 0 \end{bmatrix}.$$

For the semi-implicit line method the matrix $\hat{P}$ is given by

$$\hat{P} = \hat{\Gamma}_L + \hat{B}_a + \hat{B}_v + \hat{B}_d, \tag{17}$$

with

$$\begin{aligned} \hat{\Gamma}_L &= \frac{\Gamma}{\Delta\tau} + 2\omega_2 A_d + 2\omega_3 A_v \\ &= \begin{bmatrix} \frac{1}{\beta^2\Delta\tau} + \omega_2\frac{2\delta}{\beta_x\Delta x} & 0 & 0 \\ 0 & \frac{1}{\Delta\tau} + \omega_3\frac{2\nu}{\Delta x^2} & 0 \\ 0 & 0 & \frac{1}{\Delta\tau} + \omega_3\frac{2\nu}{\Delta x^2} \end{bmatrix}. \end{aligned}$$

For the semi-implicit point method $\hat{P}$ is equal to $\hat{\Gamma}_P$, with

$$\begin{aligned} \hat{\Gamma}_P &= \frac{\Gamma}{\Delta\tau} + 2\omega_2(A_d + B_d) + 2\omega_3(A_v + B_v) \\ &= \begin{bmatrix} \frac{1}{\beta^2\Delta\tau} + \omega_2\left(\frac{2\delta}{\beta_x\Delta x} + \frac{2\delta}{\beta_y\Delta y}\right) & 0 & 0 \\ 0 & \frac{1}{\Delta\tau} + \omega_3\left(\frac{2\nu}{\Delta x^2} + \frac{2\nu}{\Delta y^2}\right) & 0 \\ 0 & 0 & \frac{1}{\Delta\tau} + \omega_3\left(\frac{2\nu}{\Delta x^2} + \frac{2\nu}{\Delta y^2}\right) \end{bmatrix}. \end{aligned} \tag{18}$$

5.1. *Generic Test Cases*

Different flow situations are analyzed and a comparison is made between the semi-implicit point method and the semi-implicit line method. In the next figures, eigenvalues of the Fourier symbol $\mathcal{F}(\theta_x, \theta_y)$ for $\theta_x \in [0, 2\pi]$ with steps of $\Delta\theta_x = \pi/20$ and for $\theta_y = 0, \pi/2, \pi$, and $3\pi/2$ are computed and shown in the complex plane. The stepping in pseudotime is done with a four-stage method with standard coefficients. The stability domain of this method together with the eigenvalues of the Fourier symbol is shown in the left panels of the figures. In the right panels of the figures the amplification factor is shown for the algorithm using either the semi-implicit point or line method with multistage pseudotime stepping. For each (θ_x, θ_y) combination the maximum modulus of the eigenvalues of the amplification matrix is shown. All Fourier symbols and stability results are computed with *cfl*-number equal to 1.8. The same *cfl*-number is used for the experimental verification of the different test cases.

5.1.1. Inviscid flow aligned to the x-direction, grid aspect ratio $g_{ar} = 1$. Figure 2 shows good damping in the θ_x-direction for both the point and the line method. For $\theta_x = 0$ one

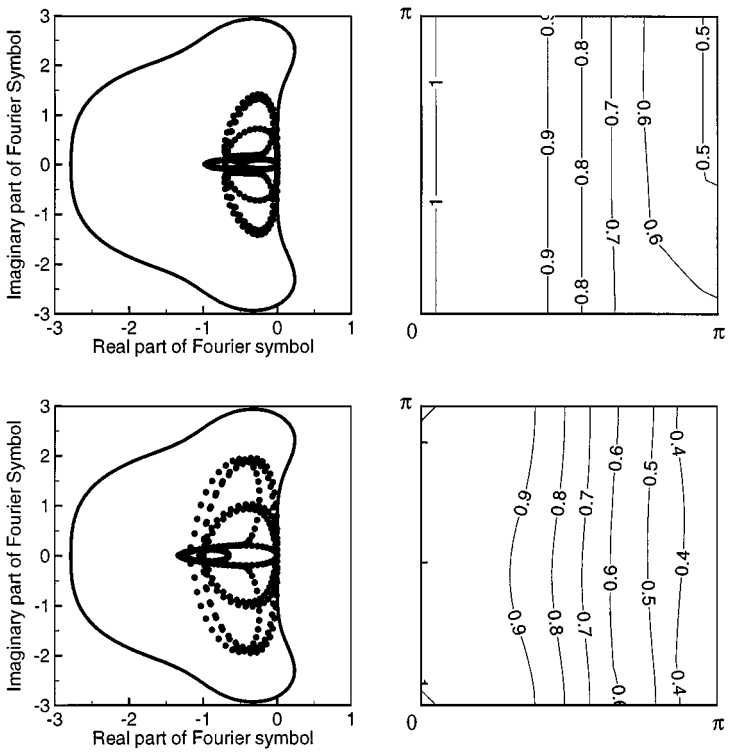

FIG. 2. Stability results for inviscid flow aligned to the x-direction, $g_{ar} = 1$; top, the point method; bottom, the line method; left, Fourier symbols in the complex plane; right, amplification factor.

eigenvalue of the $\hat{C}$ matrix of Eq. (15) becomes zero. This is due to the alignment. In this case ($\theta_x = 0$, $v = 0$) the matrix $\hat{C}$ becomes

$$\hat{C}_{\text{alignment}} = \begin{bmatrix} \frac{\delta}{\beta_y}\text{vi}(\theta_y, \Delta y)\Delta y & 0 & \text{ce}(\theta_y, \Delta y) \\ 0 & 0 & \bar{u}\text{ce}(\theta_y, \Delta y) \\ \text{ce}(\theta_y, \Delta y) & 0 & 0 \end{bmatrix}.$$

This matrix has a column of zeroes and so one eigenvalue is zero. The amplification matrix $\hat{P}^{-1}\hat{C}$ has also a zero eigenvalue and therefore its amplification factor is equal to 1. A zero eigenvalue means a loss of coupling for the correspondig eigenvector combination of the variables. This is often seen as the reason for slow convergence in aligned flow. This would mean that any flow where most of the flow field is aligned to the grid would cause slow converge. However, computations show that this is not correct.

For the experimental verification, we consider an inviscid channel flow with grid aspect ratio equal to unity. At the inlet, uniform flow is imposed and pressure is extrapolated from the flow field. At the outlet, pressure is imposed and velocity is extrapolated. At the solid walls, pressure and tangential velocity component are extrapolated and normal velocity component is set to zero. All extrapolations are done piecewise constant. As initial flow conditions, pressure is set equal to zero and velocity components equal to 0.1 of the inlet velocity. The grid has 65 nodes in the x-direction (from inlet to outlet) and also 65 nodes in the y-direction (between the two solid walls).

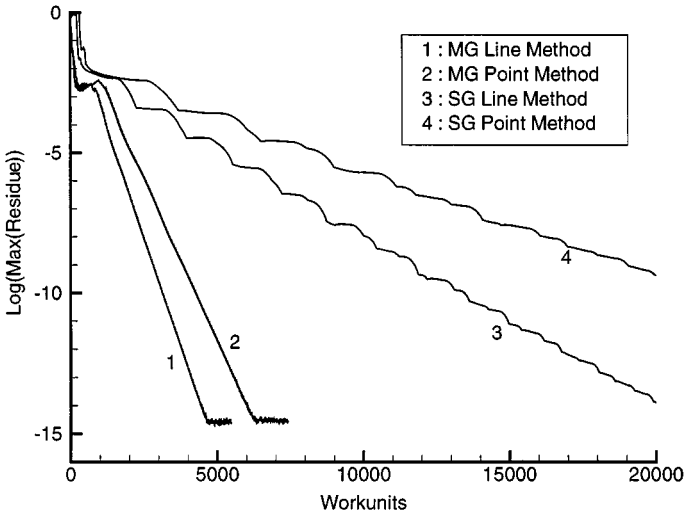

FIG. 3. Convergence results for inviscid flow aligned to the x-direction, $g_{ar} = 1$.

Figure 3 shows the convergence of the point and the line method in single grid (SG) and in multigrid formulation (MG). Five levels of grids were used in a W-cycle for the MG method.

The MG line method has the best performance in terms of work units. However, on the Cartesian grid, the cost of a flux evaluation is very low with respect to the cost the calculation of an update. Therefore the MG point method is almost three times faster in CPU than the MG line method.

The good performance in the aligned case comes from the role of the boundary conditions. Dirichlet boundary conditions are used here. The Dirichlet boundary condition at the inlet for velocity components and the Dirichlet boundary condition at the outlet for pressure together with the strong coupling of the variables in the flow direction eliminate the unsmoothed eigenvector combination. This effect is not visible in the Fourier analysis, which assumes periodic boundaries. The strong coupling in the flow direction is a consequence of the preconditioning. As already remarked, by proper choice of β, the eigenvalues of (4) can be in the same order of magnitude. In this case, the Fourier symbols for given θ_y all come together for $\theta_x = \pi$ in a zone where good damping can be assured as is clear in Fig. 2.

This can also explain why in compressible flow any local time-marching method works well as long as the Mach number is high enough. In low-Mach-number flow the convective eigenvalues are scaled down with respect to the acoustic eigenvalues and the convergence is deteriorated. However, with appropriate preconditioning the problem can be solved, despite the fact that in aligned flow the eigenvalues in the normal direction still have a different order of magnitude.

5.1.2. Inviscid flow aligned to the x-direction, grid aspect ratio $g_{ar} = 1000$. Figure 4 shows the stability results for this flow situation. Due to the high grid aspect ratio, the time step is reduced for the point method because of the stability restriction due to the acoustic system in the y-direction. This was already discussed in Subsection 4.2. In the whole (θ_x, θ_y) plane the amplification factor is around unity. The convergence will be strongly deteriorated. If the line method is used with lines in the direction of the smallest grid size (y-direction),

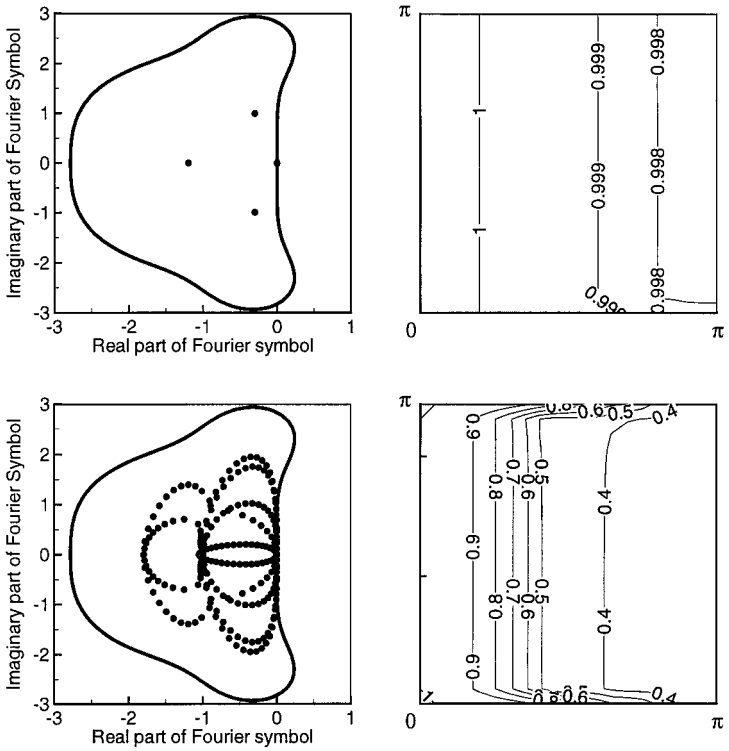

FIG. 4. Stability results for inviscid flow aligned to the x-direction, $g_{ar} = 1000$; for caption see Fig. 2.

the influence of the grid aspect ratio disappears completely. Convergence for this case is comparable to the case with grid aspect ratio equal to unity.

Figure 5 shows the convergence results for this test case. As initial flow, u-velocity is set equal to 0.1 and v-velocity equal to $0.1/g_{ar}$ of the inlet velocity. The MG and SG line

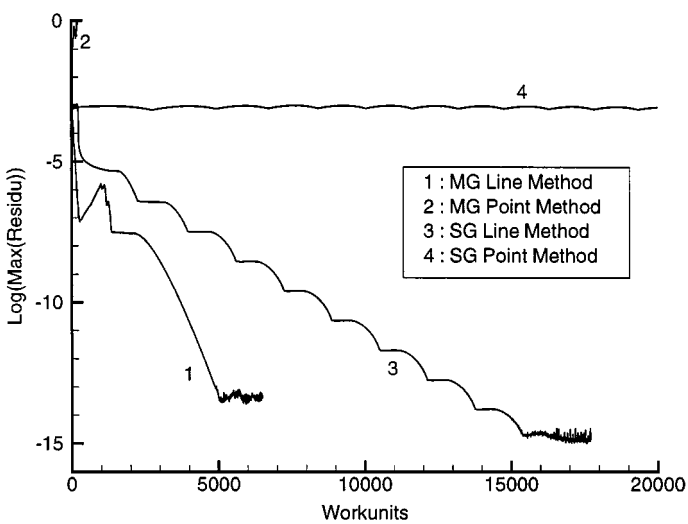

FIG. 5. Convergence results for inviscid flow aligned to the x-direction, $g_{ar} = 1000$.

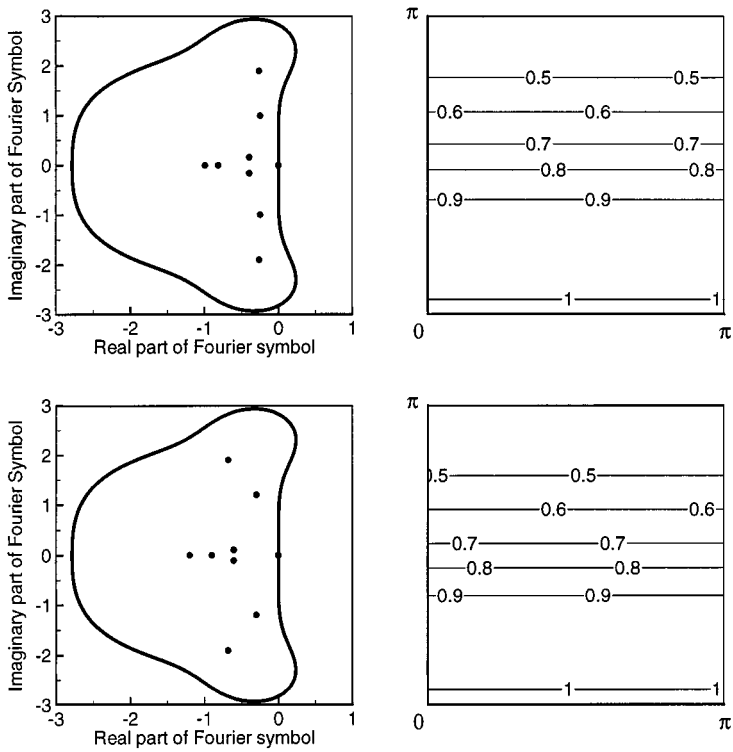

FIG. 6. Stability results for inviscid flow aligned to the y-direction, $g_{ar} = 1000$; for caption see Fig. 2.

methods perform very well as expected. The point method shows almost no convergence and its MG formulation diverges because there is no smoothing at all.

5.1.3. Inviscid flow, aligned to the y-direction, grid aspect ratio $g_{ar} = 1000$. Figure 6 shows that both the point and the line method give good damping in the streamwise direction.

The determination of the pseudotime step by (9) is in this case strongly dependent on the convective velocity component v. We observed that the line method was stable for a *cfl*-number equal to 1. However, by taking the *cfl*-number equal to 1.8 corresponding with the previous test cases, the line method became unstable. By setting the scaling factor $\omega_1 = 2$, the instability disappeared. As already mentioned above, there is a different scaling of the convective terms u and v for the line method due to the different treatment of both velocities in the computation of the pseudotime step (9). The introduction of the scaling factor can be seen as a tuning of the global *cfl*-number to the *cfl*-number for the convective subsystem in the y-direction.

The convergence plots for this test case are shown in Fig. 7. There is almost no difference between the point and the line methods. There is only an acceleration of the MG method for the first residual drop of six orders of magnitude. Then there is a breakdown of the MG performance with respect to the SG performance.

5.1.4. Viscous flow, aligned to the x-direction, grid aspect ratio 1000, $Re_{\Delta x} = 100$. Figure 8 shows that for the point method in this case, good damping is obtained in the y-direction. In the streamwise direction, there is no damping due to the small time step. As explained in Subsection 5.1.1 by using a Dirichlet boundary condition in the y-direction, good convergence can be obtained. However, pressure boundary conditions at solid walls

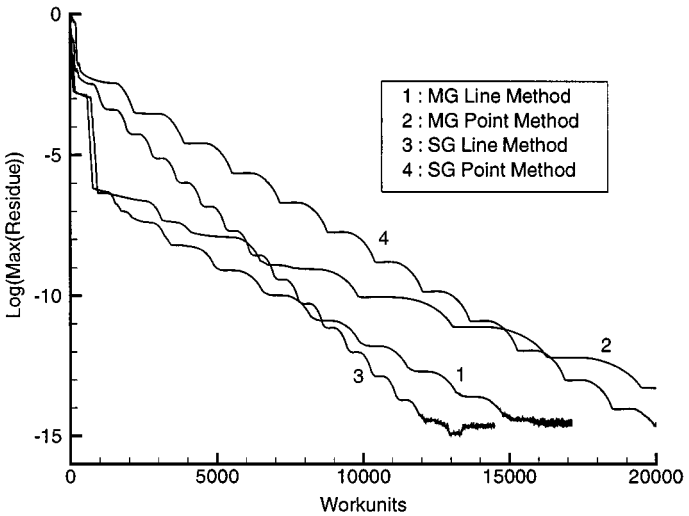

FIG. 7. Convergence results for inviscid flow aligned to the y-direction, $g_{ar} = 1000$.

are of Neumann type. The pressure level on lines in the y-direction has to be determined by information exchange along the x-direction but since there is no damping in this direction, convergence will be deteriorated. For the line method, the time step can be taken much larger so that there is very good damping in both directions.

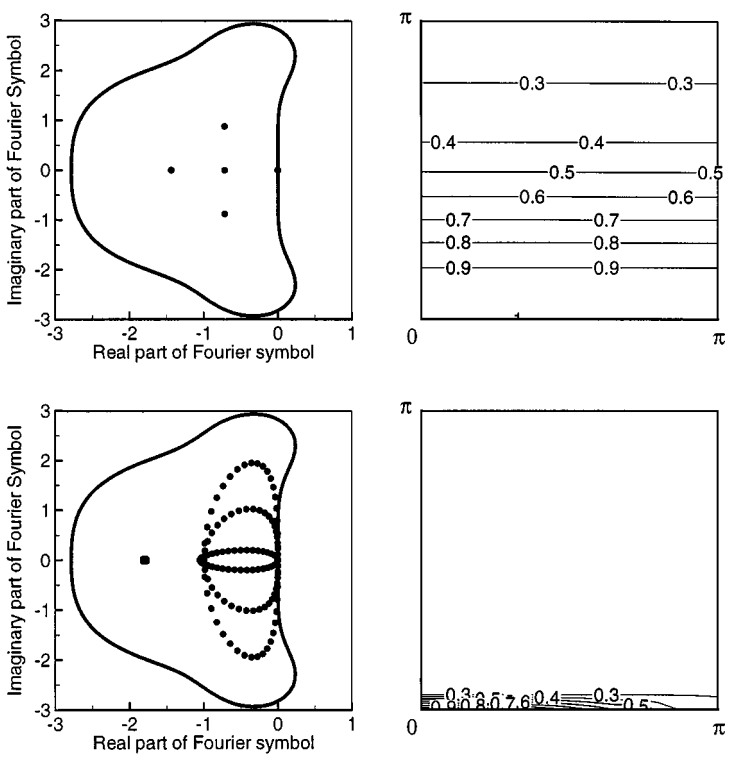

FIG. 8. Stability results for viscous flow aligned to the x-direction, $g_{ar} = 1000$, $\mathrm{Re}_{\Delta x} = 100$; for caption see Fig. 2.

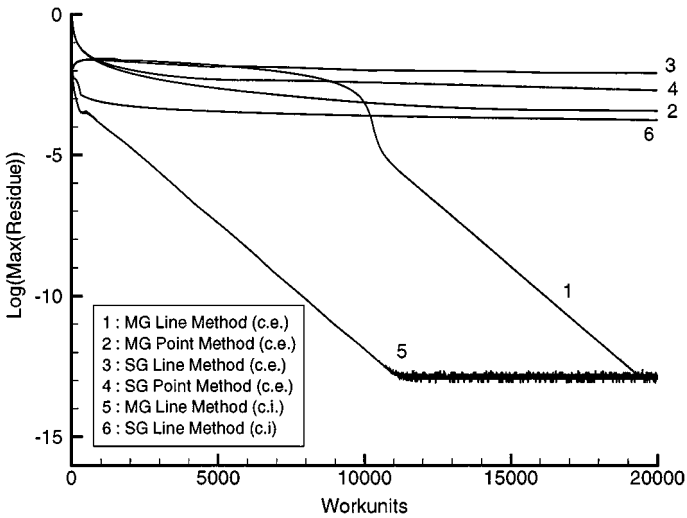

FIG. 9. Convergence results for viscous flow aligned to the x-direction, $g_{ar} = 1000$ in the whole flow field; c.e., explicit discretization of convective terms; c.i., implicit discretization of first-order part of convective terms.

For the experimental verification, at the lower boundary, the velocity is set to zero. At the upper wall a symmetry plane is assumed. So for this wall, the same boundary conditions hold as in the previous cases. At the inlet, a parabolic inlet profile is prescribed. For the construction of the grid, we consider two cases. The first grid has a grid aspect ratio equal to 1000 in the whole domain. The second grid has a grid aspect ratio equal to 1000 at the lower wall but is stretched towards the upper wall, where it has a grid aspect ratio equal to 1. As the initial flow condition, pressure and velocity are set equal to zero.

Figure 9 shows the convergence plots for the first grid. The MG line method with explicit discretization of the convective terms shows a slow convergence in the beginning. This is due to the fact that during the initial convergence phase the velocity in the field is not aligned with the grid and that in this temporary flow direction no Dirichlet boundary conditions are present for the pressure. The difference with the previous test cases is the parabolic inlet profile, which causes rather high velocities in the y-direction in the beginning of the computation. For instance, when v becomes only one-tenth of u, then the flow is to be seen as almost aligned with the y-direction because

$$\frac{v}{u}\frac{\Delta x}{\Delta y} = 100 \gg 1.$$

In that case there is no good damping in the x-direction, i.e., the direction normal to the flow (smoothing is given by Fig. 6 when θ_x- and θ_y-axes are exchanged). The lack of smoothing in the x-direction is due to the fact that the convective terms are treated explicitly, also in the line method. Therefore, if there is an important v-velocity component, the time step is restricted by this v-component (9), and causes a small *cfl*-number in the x-direction. Only if the flow is sufficiently aligned in the x-direction, the *cfl*-number in the x-direction is high enough to allow good smoothing. This happens in the test case when the residual has dropped a few orders of magnitude. From this point, the residual shows normal convergence behaviour. In order to avoid this problem, the first-order part of the convective terms can be linearized and treated implicitly in the line method (c.i. in Fig. 9). There is a gain in work units but no gain is achieved in terms of CPU for this test case, because the disadvantage with implicit

treatment of convective terms is the recalculation of the LU-decomposition of the block-tridiagonal system. With explicit treatment of the convective terms, only the backsubstitution is calculated every iteration. The reason is that, apart from the preconditioning matrix, all matrices in the left-hand side are constant. After a few initial iterations, the preconditioning matrix can be frozen and the LU-decomposition does not have to be recalculated. The saving in computing time using the latter approach will be illustrated in Section 6. Therefore we do not consider the inclusion in the left-hand side of the non-linear convective terms in the y-direction. This would only give an improvement for the very particular test case treated here, but is not necessary in more general flow situations.

As already discussed above, there is a strong coupling in the y-direction due to the high grid aspect ratio. The amplification factor is significantly below unity, compared with Fig. 4, due to the importance of the viscous terms. However, the pressure boundary condition in this direction is a Neumann boundary condition both on the lower and the upper wall. Therefore the pressure offset for this line is determined by the neighbouring lines in the x-direction, where there is a very weak coupling for the point method. This explains why the convergence is deteriorated for the point method.

A flow situation, where the grid has a constant aspect ratio along the total height, is very rare. Mostly stretched grids are used with a high aspect ratio at the boundaries, but a normal aspect ratio in the middle of the flow field. The convergence results for the same test case, but with the second grid, are shown in Fig. 10. In the region of the high aspect ratio at the lower wall, there exists a strong coupling in the y-direction and so good damping in the y-direction is obtained. In the region with smaller grid aspect ratio, there is damping in all directions. Therefore the pressure level is in this case determined by information exchange along the x-direction. This region then acts as a Dirichlet boundary condition for the underlying region with high grid aspect ratio. Therefore the convergence is good, and even the point method converges.

5.1.5. Viscous stagnation zone, grid aspect ratio $g_{ar} = 1$. We consider now $u = v = 0$. Figure 11 shows good damping in the x- and the y-direction for both the point and the line

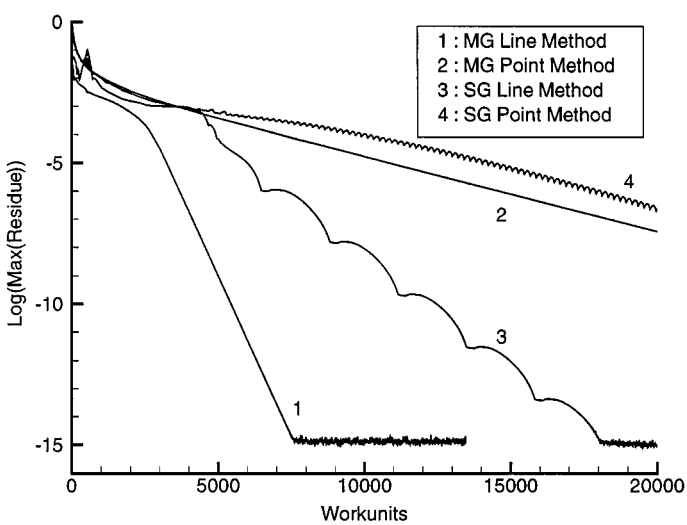

FIG. 10. Convergence results for viscous flow aligned to the x-direction, $g_{ar} = 1000$ at lower wall; $g_{ar} = 1$ at upper wall.

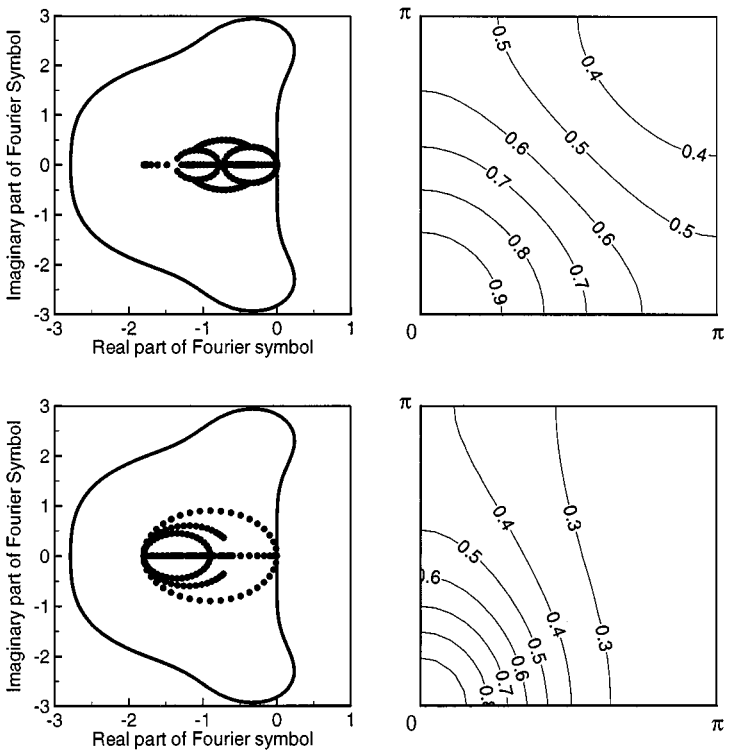

FIG. 11. Stability results for viscous stagnation zone, $g_{ar} = 1$; for caption see Fig. 2.

method. For stability reasons, the scaling factors ω_2 and ω_3 are chosen equal to 1.5 and 1, respectively, for the point method. For the line method both ω_2 and ω_3 are chosen equal to 1. The introduction of these scaling factors is needed because the viscous terms have another scaling in the Fourier space than do the convective terms. The global *cfl*-number of 1.8 is in this way tuned to an appropriate *cfl*-number for the artificial damping and viscous terms. The use of the term *cfl*-number seems to be a little strange for viscous terms, but in fact, if a local diffusion velocity is seen as

$$v_{\text{diff}} = \frac{2\nu}{\Delta x},$$

then a *cfl*-number computed on this velocity is equal to the viscous Von Neumann number σ

$$cfl = \frac{v_{\text{diff}}\Delta\tau}{\Delta x} = \frac{2\nu\Delta\tau}{\Delta x^2} = \sigma.$$

We first explain the choice of ω_2 and ω_3 for the point method. With $u = v = 0$ and for $\theta_x = \theta_y = \pi$ the matrices $\hat{P}$ (18) and $\hat{C}$ (16) are given by

$$\hat{P} = \begin{bmatrix} \frac{1}{\nu}\left(\frac{1}{2} + \omega_2\right) & 0 & 0 \\ 0 & 2\nu(1+\omega_3)\left(\frac{1}{\Delta x^2} + \frac{1}{\Delta y^2}\right) + \frac{4\nu}{\Delta x \Delta y} & 0 \\ 0 & 0 & 2\nu(1+\omega_3)\left(\frac{1}{\Delta x^2} + \frac{1}{\Delta y^2}\right) + \frac{4\nu}{\Delta x \Delta y} \end{bmatrix}$$

and

$$\hat{C} = \begin{bmatrix} \frac{2}{\nu} & 0 & 0 \\ 0 & 4\nu\left(\frac{1}{\Delta x^2} + \frac{1}{\Delta y^2}\right) & 0 \\ 0 & 0 & 4\nu\left(\frac{1}{\Delta x^2} + \frac{1}{\Delta y^2}\right) \end{bmatrix}. \tag{19}$$

For a high grid aspect ratio and with $\omega_2 = 1.5$ and $\omega_3 = 1$, $-\hat{P}^{-1}\hat{C}$ is given by

$$-\hat{P}^{-1}\hat{C} = \begin{bmatrix} -1 & 0 & 0 \\ 0 & -1 & 0 \\ 0 & 0 & -1 \end{bmatrix}, \tag{20}$$

so that for a global *cfl*-number of 1.8 all eigenvalues lie together in the complex plane in point $(-1.8, 0)$, where there is good damping. For a grid aspect ratio equal to 1, $-\hat{P}^{-1}\hat{C}$ is given by

$$-\hat{P}^{-1}\hat{C} = \begin{bmatrix} -1 & 0 & 0 \\ 0 & -\frac{2}{3} & 0 \\ 0 & 0 & -\frac{2}{3} \end{bmatrix}$$

and also in this case all eigenvalues lie in a region in the complex plane where there is good damping.

For the line method, with $u = v = 0$ and $\theta_x = \theta_y = \pi$, the $\hat{C}$-matrix is the same as (19). The $\hat{P}$-matrix (17) is given by

$$\hat{P} = \begin{bmatrix} \frac{1}{\nu}\left(\frac{3}{2} + \frac{\omega_2}{2}\right) & 0 & 0 \\ 0 & 2\nu(1+\omega_3)\frac{1}{\Delta x^2} + \frac{4\nu}{\Delta y^2} & 0 \\ 0 & 0 & 2\nu(1+\omega_3)\frac{1}{\Delta x^2} + \frac{4\nu}{\Delta y^2} \end{bmatrix}.$$

For $\omega_2 = \omega_3 = 1$, the $\hat{P}$-matrix is identical to the $\hat{C}$-matrix, so that, independent of the grid aspect ratio $-\hat{P}^{-1}\hat{C}$ is given by (20). The eigenvalues lie in a region where there is good damping for $cfl = 1.8$. We remark that the precise values of ω_2 and ω_3 are not very critical. For instance, also for the point method, good damping is obtained for $\omega_2 = \omega_3 = 1$. In fact, it is often advantageous not to choose the factors too large. It is important that the *cfl*-number can be rather large because the convergence speed is not only determined by smoothing of error components but also by elimination of these through convection out of the flow field. So, as a general rule, ω_2 and ω_3 can be set equal to unity. These values are used in the convergence tests.

Figure 12 shows the convergence plots for the viscous stagnation zone. As initial flow conditions, the pressure is set to zero and the velocity components to $0.1\nu/\Delta x$. A no slip condition on velocity is used at the left, the lower, and the upper wall. The pressure is prescribed at the right wall (maximum x). Both the point and the line methods are performing very well. The MG formulation of both methods is very effective. This is not surprising because in this case the equations are almost reduced to the equations of Laplace, for which the MG is known to work very well.

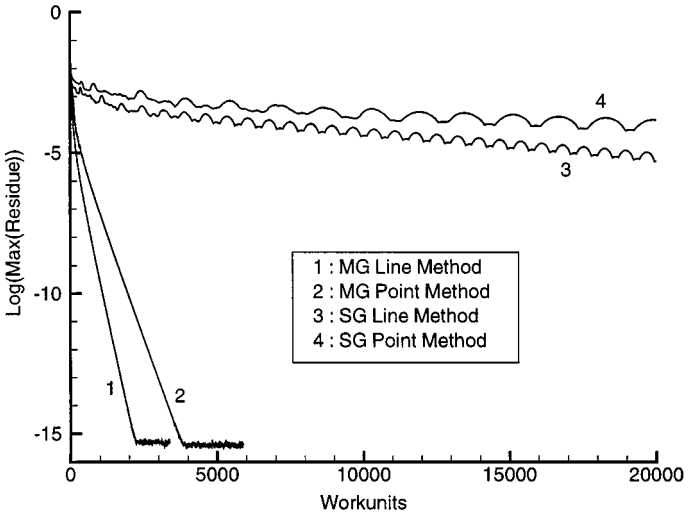

FIG. 12. Convergence results for viscous stagnation zone, $g_{ar} = 1$.

5.1.6. Viscous stagnation zone, grid aspect ratio $g_{ar} = 1000$. Again, in the Fourier analysis the scaling factors are set to $\omega_2 = 1.5$ and $\omega_3 = 1$ for the point method and to $\omega_2 = \omega_3 = 1$ for the line method.

Figure 13 shows that there is only damping in the y-direction for the point method. For the line method there is good damping in both directions.

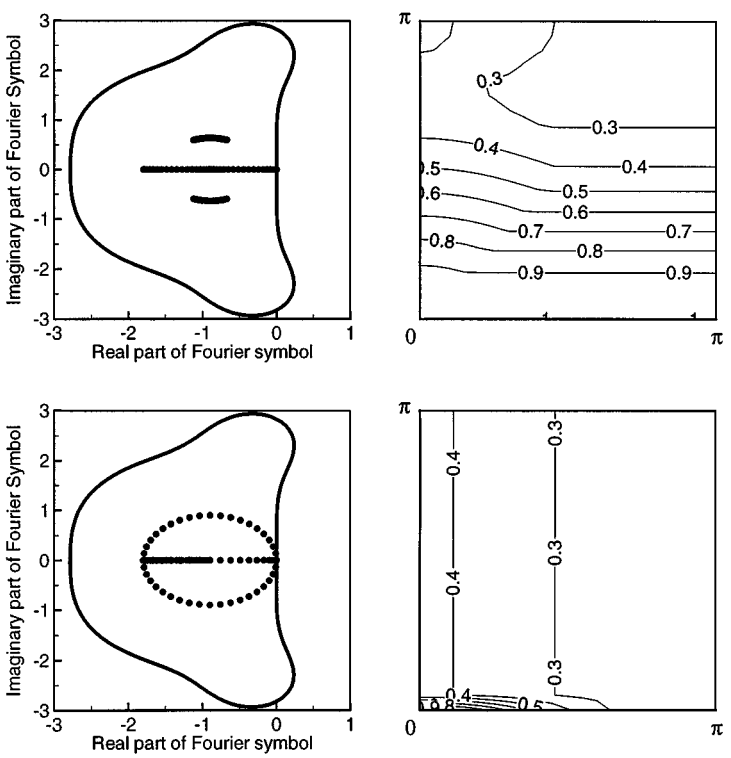

FIG. 13. Stability results for viscous stagnation zone, $g_{ar} = 1000$; for caption see Fig. 2.

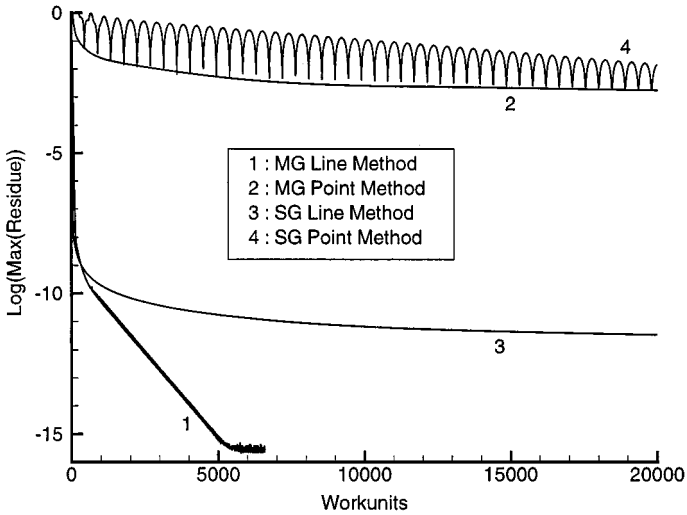

FIG. 14. Convergence results for viscous stagnation zone, $g_{ar} = 1000$.

The experimental verification in Fig. 14 shows a bad convergence for the point method. As initial flow conditions, the pressure is set to zero, the u-velocity component to $0.1\nu/\Delta x$, and the v-velocity component to $0.1\nu/\Delta y$. A no slip condition on velocity is used at the left, the lower, and the upper wall. Pressure is prescribed at the right wall (maximum x). There is a good damping in the y-direction but in this direction the boundary condition for the pressure is a Neumann boundary condition. Therefore the convergence is deteriorated. The line method shows a good convergence. This is expected because of the good damping in both directions.

6. BACKWARD FACING STEP

The method is tested on a backward facing step problem. The height of the step is chosen as one third of the channel height. We consider two grids. The first grid has 81×49 nodes and the second grid has 81×193 nodes. Both grids have the same distribution of points in the x-direction. In the y-direction the second grid has four times more cells than the first one. The highest aspect ratio on the first grid is about 35 and on the second grid 140. The same multigrid method is used as described above, but only four levels of grids are used instead of five.

Figure 15 shows the streamline pattern, obtained on the first grid, for Reynolds number

$$Re_h = \frac{U_{max} h}{\nu} = 150,$$

where h is the height of the step and U_{max} is the maximum value of the velocity at the inlet section. The streamlines were obtained by integration of the calculated velocity profiles and made dimensionless by dividing by the inlet flow rate, so that the streamline corresponding with the upper wall has the value 1. The reattachment length to step height ratio is about 6. This result is in accordance with the experimental value [14].

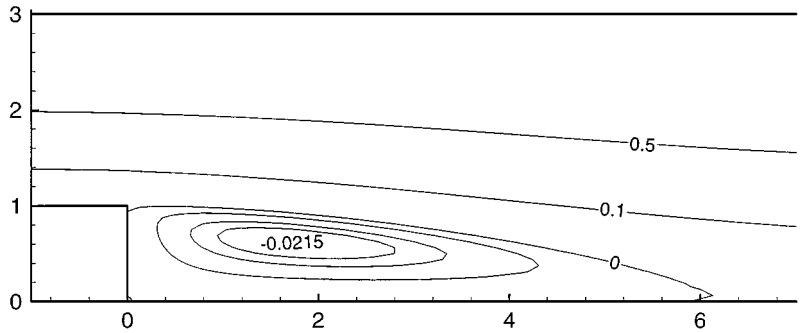

FIG. 15. Streamline pattern for the backward facing step problem, obtained at the finest grid.

Figure 16 shows the isobars, normalized according to

$$\bar{p} = Re_h \frac{p - p_c}{1/2\rho U_{max}^2}, \tag{21}$$

where p_c is the corner pressure.

Figure 17 shows the convergence history for the MG point and the MG line method on the two grids with different grid aspect ratios. It is clear that for the line method the grid aspect ratio has no influence on the performance of the method, while for the point method the convergence deteriorates when the grid aspect ratio becomes larger. The asymptotic convergence rate for the line method is 0.5062 per MG cycle.

The computational cost is extremely low for this method. When the residual drops a few orders of magnitude, the non-linear local preconditioning matrix can be kept fixed. All other terms in the left-hand side of the system (7) are linear terms. This means that the LU-decomposition for solving the tridiagonal block system can be stored in memory for the different levels of grids. The computational cost for a flux evaluation is also very low since the Jacobians of the linear terms are also stored. Therefore, for one time step, only the non-linear convective contributions are recomputed and only a backsubstitution is computed for the evaluation of one step in the multistage scheme. The gain in performance using this approach is shown in Fig. 18.

7. COMPRESSIBLE FLOW

The compressible equations are given by

$$\frac{\partial F_{nv}}{\partial x} + \frac{\partial G_{nv}}{\partial y} - \frac{\partial F_v}{\partial x} - \frac{\partial G_v}{\partial y} = 0,$$

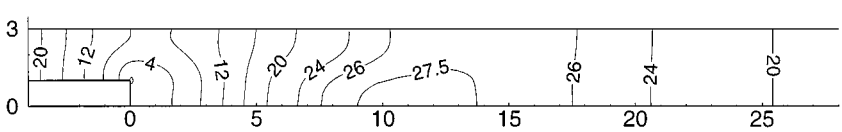

FIG. 16. Isobar contours for the backward facing step problem.

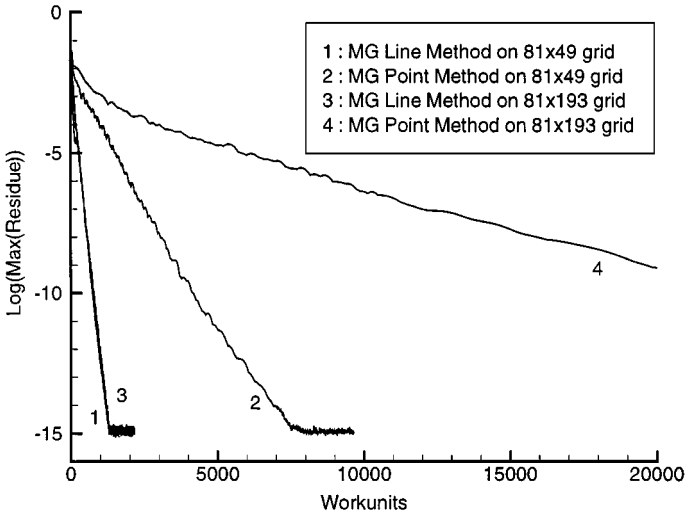

FIG. 17. Convergence results for the backward facing step problem, comparison of the MG point and the MG line method on two different grids.

with

$$F_{nv} = \begin{pmatrix} \rho u \\ \rho uu + p \\ \rho uv \\ \rho uH \end{pmatrix}, \qquad G_{nv} = \begin{pmatrix} \rho v \\ \rho uv \\ \rho vv + p \\ \rho vH \end{pmatrix},$$

$$F_v = \begin{pmatrix} 0 \\ \tau_{xx} \\ \tau_{xy} \\ u\tau_{xx} + v\tau_{xy} + q_x \end{pmatrix}, \qquad G_v = \begin{pmatrix} 0 \\ \tau_{yx} \\ \tau_{yy} \\ u\tau_{yx} + v\tau_{yy} + q_y \end{pmatrix}.$$

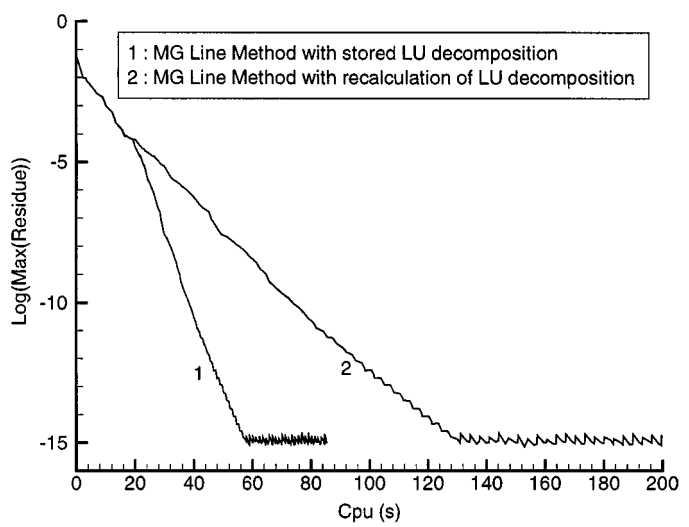

FIG. 18. Convergence results for the backward facing step problem, MG line method with recalculation of the LU-decomposition every time step, compared with storage of the LU-decomposition after an initial phase.

where $\underline{\underline{\tau}}$ is the stress tensor and $\underline{q}$ is the heat flux vector. H is the total enthalpy given by

$$H = \frac{\gamma}{\gamma - 1}\frac{p}{\rho} + \frac{1}{2}(u^2 + v^2).$$

7.1. *Preconditioning*

The method described for incompressible flow can easily be extended to low-Mach-number flow. The artificial-compressibility method causes the convective and pseudo-acoustic wave speeds to be in the same order of magnitude. Therefore, for compressible flow, any preconditioner can be used which also scales the convective and the acoustic speeds. We used a preconditioner based on Weiss and Smith's preconditioner [17],

$$\Gamma = \begin{bmatrix} \Theta & 0 & 0 & \rho_T \\ \Theta u & \rho & 0 & \rho_T u \\ \Theta v & 0 & \rho & \rho_T v \\ \Theta H - 1 & \rho u & \rho v & \rho_T H + \rho C_p \end{bmatrix},$$

where $\Theta = 1/\beta^2 - \rho_T/\rho C_p$. This preconditioner is equivalent to the extension of the Chorin preconditioner [3] to compressible flow applications by Turkel [4, 16], but is formulated in the so-called viscous variables: $Q_v = [p \;\; u \;\; v \;\; T]^T$, where T denotes the temperature and ^{T} the transposed vector. C_p is the specific heat at constant pressure and ρ_T is the derivative of ρ with respect to T.

We simplified the preconditioner by setting to zero the terms with velocity components. By doing this, the eigenvalues of the preconditioned system are still of the same order of magnitude, but they cannot be written analytically. Further, for small velocities, so for small β, θ can be approximated by $1/\beta^2$ and $\Theta H - 1 \approx \Theta H$.

The final preconditioner used for the compressible system is

$$\Gamma = \begin{bmatrix} \Theta & 0 & 0 & \rho_T \\ 0 & \rho & 0 & 0 \\ 0 & 0 & \rho & 0 \\ \Theta H & 0 & 0 & \rho_T H + \rho C_p \end{bmatrix}, \tag{22}$$

where $\Theta = 1/\beta^2$. With this form of the preconditioner a comparison between incompressible flow and low-Mach-number compressible flow can be made directly.

It is clear that the momentum equations update the velocity components, as for incompressible flow. The relative importance of the temperature update in the energy equation with respect to the temperature update in the continuity equation is given by

$$\frac{\Gamma_{44}/\Gamma_{41}}{\Gamma_{14}/\Gamma_{11}} = \frac{\rho_T H + \rho C_p}{\Theta H} \Big/ \frac{\rho_T}{\Theta} \approx \frac{\gamma - 1}{2} M^2,$$

where M is the Mach number. This shows that in the low-Mach-number limit the energy equation updates the pressure with this kind of preconditioning. Once the pressure update is known, the continuity equation updates the temperature. This is only true for inviscid flow, because due to the implicit treatment of the temperature diffusion term for viscous flow, both the continuity equation and the energy equation update a combination of temperature and pressure.

7.2. *Discretization*

7.2.1. Inviscid subsystem. As for incompressible flow, the convective part of the momentum equation is discretized with velocity upwinding:

$$F_{c_{i+1/2}} = u_{i+1/2} \begin{bmatrix} 0 \\ \rho u \\ \rho v \\ 0 \end{bmatrix}_{L/R}, \qquad G_{c_{j+1/2}} = v_{j+1/2} \begin{bmatrix} 0 \\ \rho u \\ \rho v \\ 0 \end{bmatrix}_{L/R}.$$

The pressure term in the momentum equations and the velocity terms in the continuity and energy equations are treated like the pseudo-acoustic part in incompressible flow and are discretized centrally.

In the previous section it was shown that for small velocities, the energy equation is updating the pressure in pseudotime. Therefore, by comparison with incompressible flow, the question can be raised if the energy equation also expresses that the divergence of the velocity field $\nabla \cdot \underline{u}$ goes towards zero for small velocities. The momentum equation causes a scaling of ∇p with a factor M^2. This is true even if the density does not scale with the Mach number, which can be the case across streamlines. The energy equation can be written as

$$\nabla \cdot (\rho H \underline{u}) = \rho H \nabla \cdot \underline{u} + \underline{u} \cdot \nabla(\rho H) = 0, \tag{23}$$

with $\rho H = \frac{\gamma}{\gamma - 1} p + 1/2 \rho \underline{u}^2$, and $\gamma = C_p / C_v$, where C_v is the specific heat at constant temperature.

Since $\nabla(\rho H)$ is proportional to ∇p for vanishing velocity, the second term in (23) scales with M^3 so that also $\nabla \cdot \underline{u}$ scales with M^3. This shows that the energy equation expresses that $\nabla \cdot \underline{u}$ is going to zero. So, the energy equation for low-Mach-number compressible flow takes over the role of the continuity equation for incompressible flow. Further we remark that from the continuity equation

$$\nabla \cdot (\rho \underline{u}) = \rho \nabla \cdot \underline{u} + \underline{u} \cdot \nabla \rho = 0$$

follows that differences in density scale with M^2 along streamlines.

Therefore the dissipation term that was introduced in the continuity equation for incompressible flow has to be introduced in the energy equation for low-Mach-number compressible flow. For dimensional reasons it must be multiplied with enthalpy,

$$F_{d1_{i+1/2}} = \delta \begin{bmatrix} 0 \\ 0 \\ 0 \\ H_{i+1/2} \frac{p_{i+1} - p_i}{\beta_x} \end{bmatrix},$$

where β_x is given by $\beta_x = w_r + \frac{2\nu}{\Delta x}$ as for incompressible flow. Again w_r can be chosen either as a global velocity or as a local velocity. A similar expression holds for $G_{d1_{j+1/2}}$.

In the previous section was shown that with the current preconditioner (22) the continuity equation causes an update for temperature. Therefore we have to add a temperature dissipation term in the continuity equation. By doing this, the physical diffusion term of temperature in the energy equation will not be disturbed.

Analytically, the continuity equation scales with M^3. However, due to the introduction of the dissipation term for the pressure in the energy equation, only the sum of the divergence of the velocity field and the dissipation term for pressure scales with M^3. Therefore the same dissipation term for pressure has to be added to the continuity equation. The dissipation term for the temperature is multiplied with a velocity coefficient, since it has to scale with M^3. No temperature dissipation is allowed across streamlines in an aligned flow. So, a good choice of the velocity coefficient is the normal projection of the local velocity on the edge of the control volume. In order to make the temperature dissipation term dimensionally correct it is multiplied with ρ_T. In this way the ratio of pressure and temperature dissipation terms corresponds with the ratio of pressure and temperature updates given by the preconditioner,

$$F_{d2_{i+1/2}} = \delta \begin{bmatrix} \frac{p_{i+1} - p_i}{\beta_x} + |u|\rho_T (T_{i+1} - T_i) \\ 0 \\ 0 \\ 0 \end{bmatrix}.$$

$G_{d2_{j+1/2}}$ is computed in a similar way.

If the dissipation term for pressure in the continuity equation did not correspond to the dissipation term in the energy equation, it would not be possible to obtain a temperature field that scales with M^2 for Mach numbers going to zero.

7.2.2. Viscous subsystem. The viscous subsystem is more complex for the compressible equations than for the incompressible equations. Normal derivatives are discretized as for incompressible flow. The discretization of the tangential derivatives is shown in the next example. Consider the discretization of $\frac{\partial v}{\partial y}$ along the edge $i + 1/2$ of the control volume in Fig. 1. The tangential derivative is then discretized as

$$\frac{\partial v}{\partial y} = \frac{v_{i+1/2,\,j+1/2} - v_{i+1/2,\,j-1/2}}{y_{i+1/2,\,j+1/2} - y_{i+1/2,\,j-1/2}},$$

with

$$v_{i+1/2,\,j+1/2} = \frac{1}{4}(v_i + v_{i+1} + v_{i,\,j+1} + v_{i+1,\,j+1})$$

and the other terms are computed in a similar way.

7.2.3. Discretization in pseudotime. The discretization in pseudotime is done with the preconditioner (22). The acoustic flux is treated implicitly in the direction of the shortest grid distances. Since this flux is non-linear for compressible flow, a linearization is needed. Similarly as for incompressible flow, the acoustic flux on time level $(m + 1)^*$ is written as

$$G^{(m+1)^*}_{a_{j+1/2}} = \begin{bmatrix} \rho^{(m)} v^{(m+1)^*} \\ 0 \\ p^{(m+1)^*} \\ \rho^{(m)} H^{(m)} v^{(m+1)^*} \end{bmatrix}_{j+1/2}.$$

The linearization is only valid for low-speed flow.

Finally, the normal viscous fluxes are treated like the viscous fluxes for incompressible flow. The tangential fluxes are treated explicitly.

No separate stability analysis is done for compressible flow. The *cfl*-number could not be larger than 1.6.

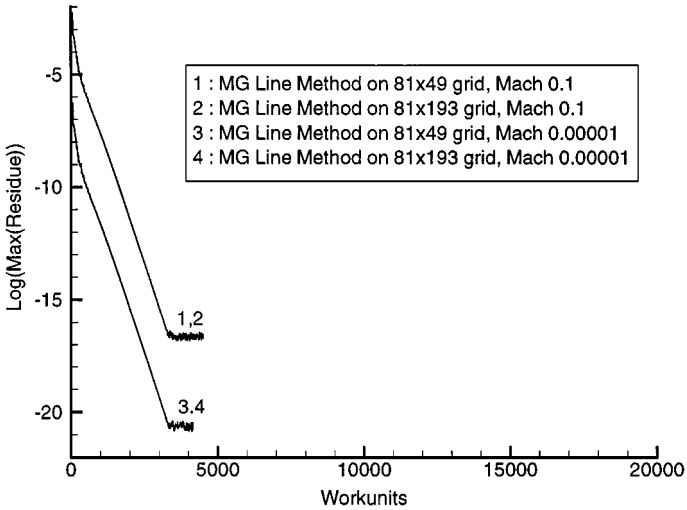

FIG. 19. Convergence results for the compressible backward facing step problem, comparison of the MG line method on two different grids for different Mach numbers.

7.2.4. Backward facing step (compressible flow). We use the same grids and the same global reference velocity w_r for the pressure dissipation term as in the incompressible test case. On each grid the flow is calculated with the semi-implicit line method for Mach 0.1 and Mach 10^{-5}. Figure 19 shows the convergence results. There is no difference in convergence behaviour between the two different grids. The difference in Mach number only causes a shift in the magnitude of the residual; convergence is achieved in an equal number of work units. The asymptotic convergence rate for all cases is 0.7455 per MG cycle.

Figure 20 shows the streamline patterns for both Mach numbers. No difference can be seen between the two patterns. There is also no difference with the streamline pattern for incompressible flow (Fig. 15).

Figure 21 shows the dimensionless isobars (21) for both Mach numbers. Again no difference can be seen with the result for incompressible flow (Fig. 16). This shows that pressure differences are scaled with M^2.

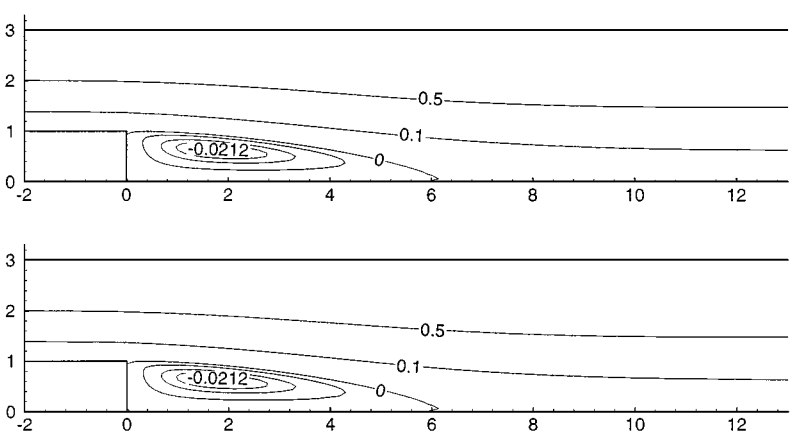

FIG. 20. Streamline pattern for the compressible backward facing step problem. Top, Mach 10^{-1}; bottom, Mach 10^{-5}.

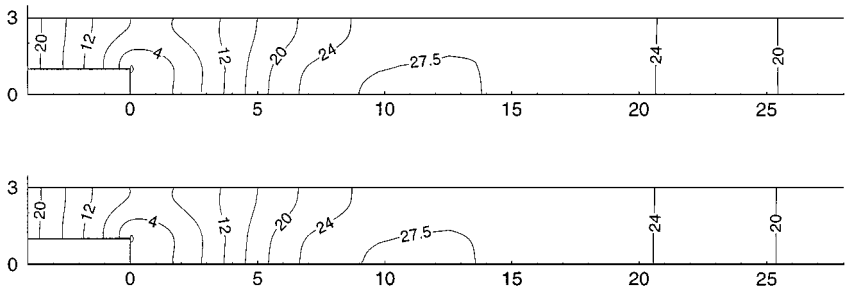

FIG. 21. Isobar contours for the compressible backward facing step problem. Top, Mach 10^{-1}; bottom, Mach 10^{-5}.

Figure 22 shows isotherms for both Mach numbers. At the inlet ($x = -10$) a uniform temperature field is prescribed. The temperatures are made dimensionless by

$$\bar{T} = Re_h \frac{R(T - T_c)}{U_{max}^2},$$

where T_c represents the temperature at the corner. From this figure it can be seen that also temperature differences are scaled with M^2.

7.2.5. Flow in a thermally driven cavity. The final test problem considers a buoyancy-driven flow in a square cavity [1, 2]. The configuration consists of two vertical walls at temperature T_h and T_c and two adiabatic horizontal walls. It is known that this problem exhibits complex flow features depending on the Rayleigh number ($Ra = \rho^2 g\beta(T_h - T_c)L^3 C_p/\mu k$), the aspect ratio of the cavity and a temperature difference parameter ($\varepsilon = (T_h - T_c)/(T_h + T_c)$). Here β is the thermal expansion coefficient, g is the magnitude of the gravitational field, L is the length of the cavity walls, and μ and k are the dynamic viscosity and thermal conductivity, respectively.

For the present study, three Rayleigh numbers, $Ra = 10^3$, 10^5, and 10^6 are considered with a temperature difference parameter $\varepsilon = 0.6$. The aspect ratio of the present problem is one and transport properties (μ and k) are evaluated by using Sutherland's law [18, 1]. The Prandtl number based on reference transport properties is 0.71. A 81×81 uniform grid and a local reference velocity w_r for the pressure dissipation term are used for all cases.

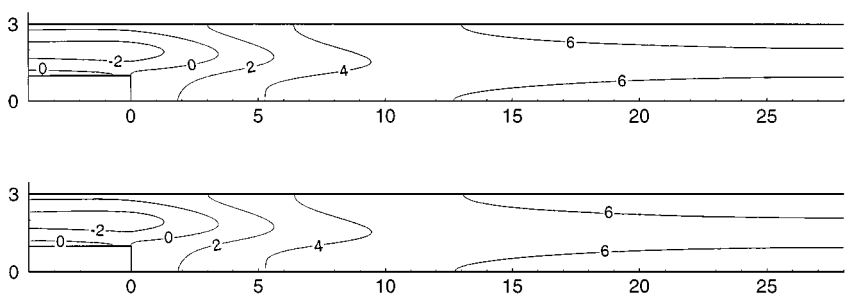

FIG. 22. Isotherm contours for the compressible backward facing step problem. Top, Mach 10^{-1}; bottom, Mach 10^{-5}.

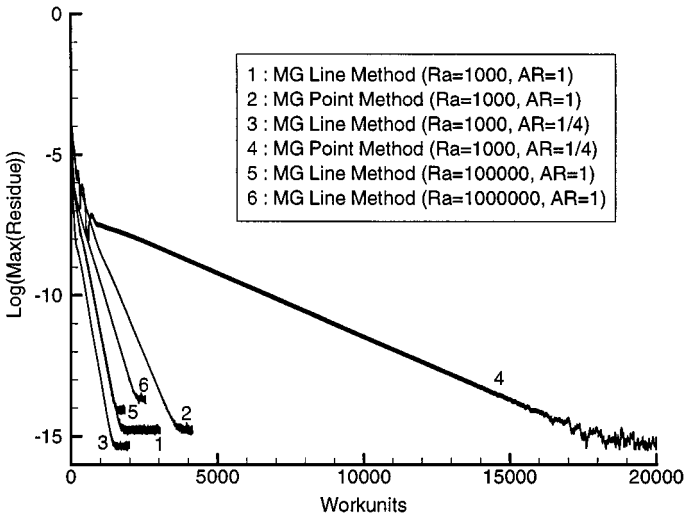

FIG. 23. Convergence results for the thermally driven cavity flow problem with $Ra = 10^3$, 10^5, and 10^6.

For $Ra = 10^3$, the convergence behaviour is compared with a calculation on a 321×81 grid (grid aspect ratio $1/4$). Convergence rates are shown in Fig. 23. The convergence behaviour for the multigrid line method was essentially independent of Rayleigh number and grid aspect ratio. The asymptotic convergence rate achieved for $Ra = 10^3$ and grid aspect ratio equal to $1/4$, is 0.7897 per MG cycle. The multigrid point method required more work units but was faster in terms of CPU for $Ra = 10^3$ with grid aspect ratio equal to one. The convergence rate for this method slowed down for $Ra = 10^3$ with grid aspect ratio equal to $1/4$.

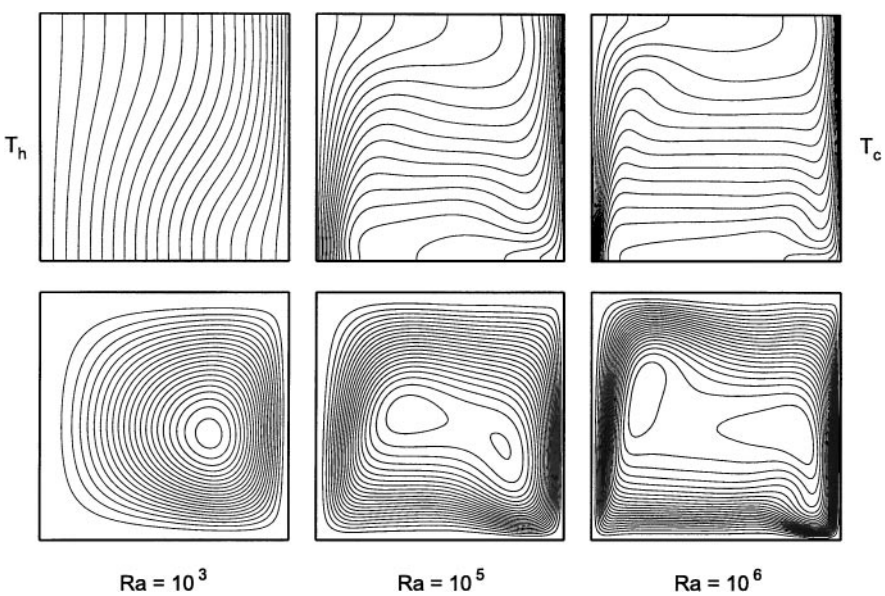

FIG. 24. Temperature isolines and streamlines for a viscous flow in a thermally driven cavity for $Ra = 10^3$, 10^5, and 10^6.

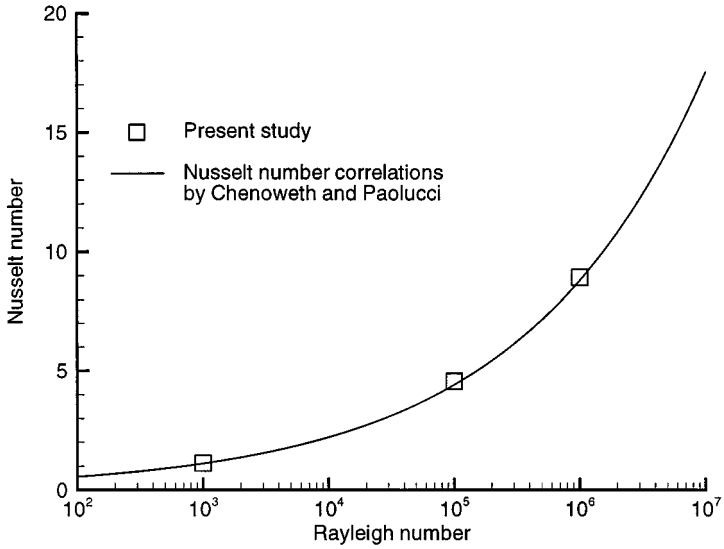

FIG. 25. Comparison of the Nusselt number with a correlation by Chenoweth and Paolucci [1].

Figure 24 shows temperature isolines and streamlines for $Ra = 10^3$, 10^5, and 10^6. The accuracy of the numerical solutions is verified by comparing the Nusselt number at the left-side wall with a correlation by Chenoweth and Paolucci [1] in Fig. 25. Good agreement can be observed for all three cases.

8. CONCLUSIONS

A method of discretization of the incompressible and low-Mach-number compressible Navier–Stokes equations is presented. The local preconditioning method is combined with a line solver in order to remove the stiffness coming from high grid aspect ratios. This line solver is used in a multistage stepping scheme and accelerated with the multigrid method. The different test cases with alignment of the flow to the grid and the use of a grid aspect ratio of 1000 show that the method is very robust and has a good performance.

As realistic flow problems, the flow through a backward facing step and the flow in a thermally driven cavity were computed. The results show that the accuracy of the discretization method is very good. The convergence of the solution method is very fast for both incompressible and low-Mach-number compressible flows, independent of the grid aspect ratio. The CPU cost of the incompressible method is extremely low, due to a cheap flux evaluation and due to the fact that the LU decomposition can be stored since all terms, which have to be treated implicitly, are linear.

REFERENCES

1. D. R. Chenoweth and S. Paolucci, Natural convection in an enclosed vertical air layer with large horizontal temperature differences, *J. Fluid. Mech.* **169**, 173 (1986).
2. Y. Choi and C. Merkle, The application of preconditioning in viscous flows, *J. Comput. Phys.* **105**, 207 (1993).
3. A. J. Chorin, A numerical method for solving incompressible viscous flow problems, *AIAA J.* **2**, 12 (1967).

4. D. L. Darmofal and B. van Leer, Local preconditioning: Manipulating mother nature to fool father time, in *Computing the Future. II. Computational Fluid Dynamics and Transonic Flow*, edited by D. Caughey and M. Hafez (Wiley, New York, 1998).
5. E. Dick and J. Linden, A multigrid method for steady incompressible Navier–Stokes equations based on flux difference splitting, *Int. J. Numer. Methods Fluids* **14**, 1311 (1992).
6. J. Edwards and M.-S. Liou, Low-diffusion flux splitting methods for flows at all speeds, *AIAA J.* **36**(9), 1610 (1998).
7. A. Godfrey, R. Walters, and B. van Leer, Preconditioning for the Navier–Stokes equations with finite rate chemistry, in *Proc. 31st Aerospace Sciences Meeting, Reno, 1993*, AIAA-93-0535.
8. B. Koren and B. van Leer, Analysis of preconditioning and multigrid for Euler flows with low-subsonic regions, *Adv. Comput. Math.* **4**, 127 (1995).
9. D. Lee, B. van Leer, and J. Lynn, A local Navier–Stokes preconditioner for all Mach and cell Reynolds numbers, in *Proc. 13th AIAA CFD Conference, Snowmass, CO* (AIAA, Washington, DC, 1997), AIAA-97-2024, p. 842.
10. W. Lee, "Local Preconditioning of the Euler Equations," Ph.D. thesis, University of Michigan, 1991.
11. M.-S. Liou and C. J. Steffen, Jr., A new flux splitting scheme, *J. Comput. Phys.* **107**, 23 (1993).
12. D. J. Mavriplis, Multigrid strategies for viscous flow solvers on anisotropic unstructured meshes, in *Proc. 13th AIAA CFD Conference, Snowmass, CO* (AIAA, Washington, DC, 1997), AIAA-97-1952, p. 659.
13. C. L. Merkle, J. Y. Sullivan, P. E. O. Buelow, and S. Venkateswaran, Computation of flows with arbitrary equations of state, *AIAA J.* **36**(4), 515 (1998).
14. E. Morgan, J. Periaux, and F. Thomasset, Analysis of laminar flow over a backward facing step, in *Notes on Numerical Fluid Mechanics* (Vieweg, Braunschweig, 1984), Vol. 9.
15. E. Turkel, A review of preconditioning methods for fluid dynamics, *Appl. Numer. Math.* **12**, 257 (1993).
16. E. Turkel, Preconditional techniques in computational fluid dynamics, *Annu. Rev. Fluid Mech.* **31**, 385 (1999).
17. J. Weiss and W. Smith, Preconditioning applied to variable and constant density flows, *AIAA J.* **33**(11), 2050 (1995).
18. F. M. White, *Viscous Fluid Flow* (McGraw–Hill, New York, 1974).